Science Advances
AAAS

advances.sciencemag.org/cgi/content/full/6/30/eabb9379/DC1

Supplementary Materials for

Accessing new magnetic regimes by tuning the ligand spin-orbit coupling in van der Waals magnets

Thomas A. Tartaglia, Joseph N. Tang, Jose L. Lado, Faranak Bahrami, Mykola Abramchuk, Gregory T. McCandless, Meaghan C. Doyle, Kenneth S. Burch, Ying Ran, Julia Y. Chan, Fazel Tafti*

*Corresponding author. Email: fazel.tafti@bc.edu

Published 24 July 2020, *Sci. Adv.* **6**, eabb9379 (2020)
DOI: 10.1126/sciadv.abb9379

This PDF file includes:

Synthesis

A chemical vapor transport technique was used to grow crystals of the VdW alloys, $CrCl_{3-x-y}Br_xI_y$, inside a tube furnace with the charge at the hot end (650 °C) and a temperature gradient of 200 °C during 72 h. The charge was a mixture of the parent compounds, $CrCl_3$, $CrBr_3$, and CrI_3 with appropriate molar ratios as summarized in Table S1 for five representative samples. The actual elemental composition of the resulting crystals was evaluated by EDX. Based on the anion sizes, we found three regimes of formation and sensitivity to air: (1) The two-halide series $CrCl_{3-x}Br_x$ and $CrBr_yI_{3-y}$ have comparable anion sizes and form readily; (2) The large size difference between Cl and I prevents the formation of $CrCl_xI_{3-x}$ series; (3) The three-halide series, $CrCl_{3-x-y}Br_xI_y$, form but are less stable in air than the two-halide series.

Table S1: Summary of the starting reaction mixture and the actual composition (from EDX) are listed for five representative samples. Statistical errors are calculated from the standard deviation of EDX spectra at several spots on each sample.

Reaction mixture	Composition according to EDX
$CrCl_3$ + 1.12 $CrBr_3$ + 1.5 CrI_3	$CrCl_{0.369(1)}Br_{1.32(1)}I_{1.31(1)}$
$CrCl_3$ + 1.3 $CrBr_3$ + 1.5 CrI_3	$CrCl_{0.428(2)}Br_{1.54(1)}I_{1.03(2)}$
1.7 $CrCl_3$ + $CrBr_3$ + 1.35 CrI_3	$CrCl_{0.846(9)}Br_{1.78(5)}I_{0.378(47)}$
1.8 $CrCl_3$ + $CrBr_3$ + 1.35 CrI_3	$CrCl_{1.03(6)}Br_{1.41(4)}I_{0.564(25)}$
3 $CrCl_3$ + $CrBr_3$ + 2.2 CrI_3	$CrCl_{0.822(2)}Br_{1.18(1)}I_{0.998(3)}$

Phase Diagram

In the main text, we focused on the triangular phase diagrams of T_C, Θ_W, and $f = \Theta_W/T_C$ with the field parallel to the honeycomb planes ($B_\parallel$). In figure S1, we present similar phase diagrams, but with field perpendicular to the planes ($B_\perp$).

Determination of T_C

The magnetic transition temperature, T_C, can be defined by referring to the peak in $\chi(T)$ or $d\chi/dT$ as shown in figure S2. Although both criteria give similar phase diagrams, we decided

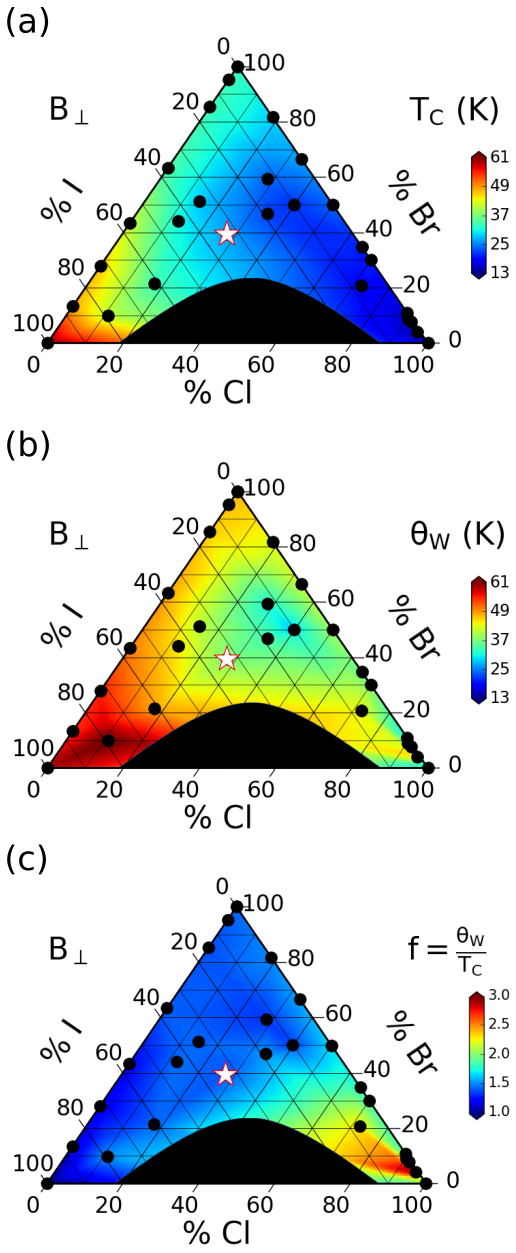

Figure S1: **Triangular phase diagrams with the field out-of-plane.** (a) Triangular phase diagram of T_C as a function of composition in $CrCl_{3-x-y}Br_xI_y$ with the magnetic field perpendicular to the honeycomb planes. (b) Triangular phase diagram of the Weiss temperature Θ_W. (c) Triangular phase diagram of the frustration index f, showing the appearance of a magnetic frustration near $CrCl_3$ and its disappearance toward $CrBr_3$ and CrI_3. The color maps are produced by a linear interpolation between the 27 discrete data points, each represented by a black dot.

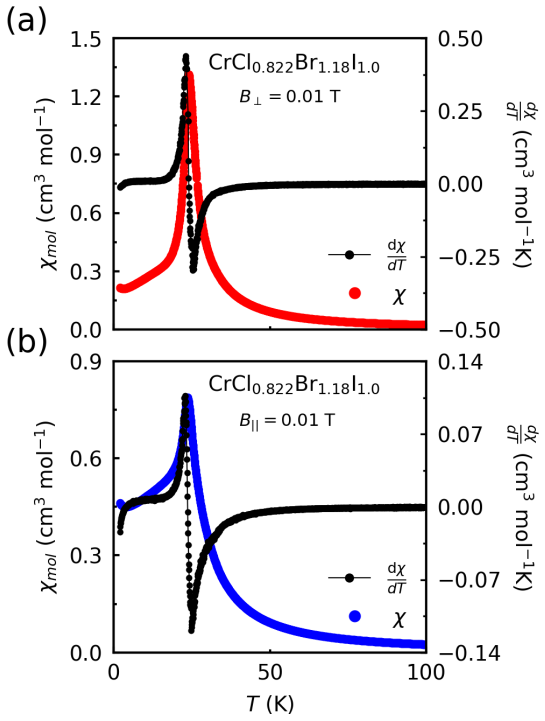

Figure S2: **Determination of T_C with different criteria.** (a) χ and $d\chi/dT$ as a function of temperature for $B_\perp$. (b) χ and $d\chi/dT$ as a function of temperature for $B_\parallel$.

to use the latter, because the peak in $d\chi/dT$ is sharper than the one in $\chi(T)$. The uncertainty was defined based on the full-width at half-maximum (FWHM) which was smaller in $d\chi/dT$ by only a few percents.

Curie-Weiss Analysis

In the main text, we showed the Curie-Weiss analysis for $CrCl_{0.8}Br_{1.2}I_{1.0}$, which was the closest sample to the center of the triangular phase diagrams. In figure S3, we present the CW analysis for nine additional representative samples with in-plane field.

Density Functional Theory

The magnetic anisotropy calculations were performed with the all-electron LAPW formalism implemented in the Elk code (42). Before calculating the anisotropy energy, we performed a

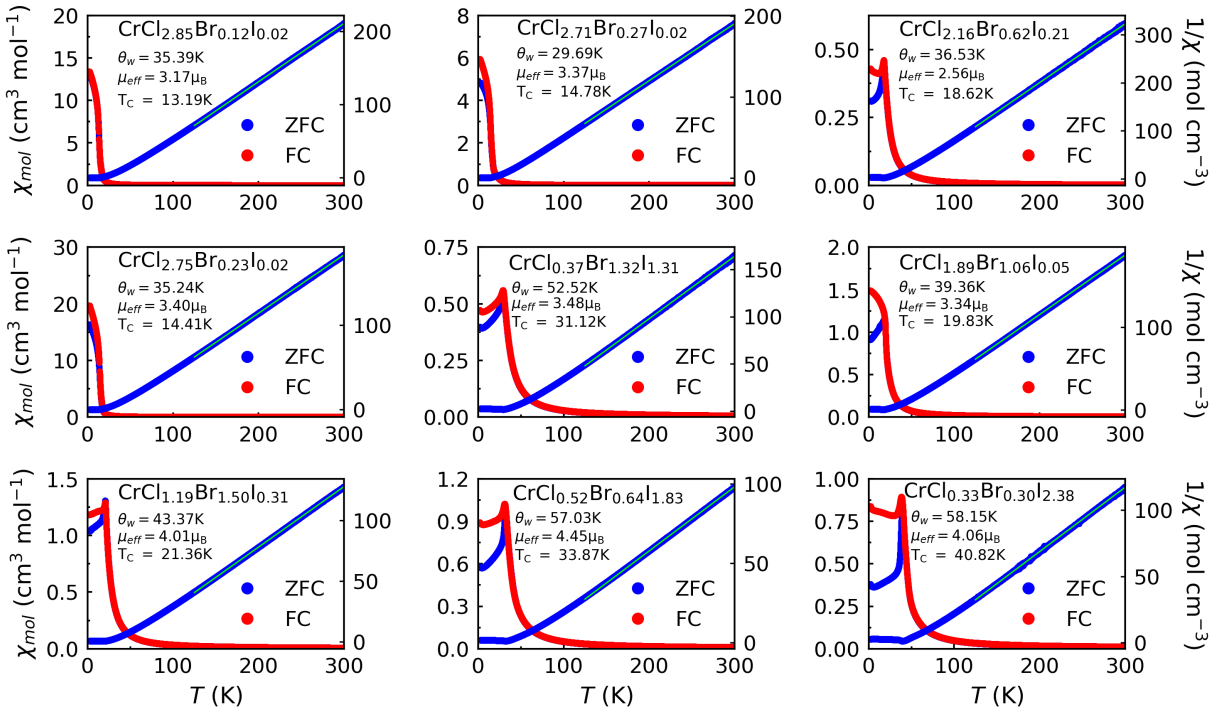

Figure S3: **Magnetic susceptibility data for different compositions.** Susceptibility as a function of temperature for nine representative samples in the $B_{||}$ configuration. Both the zero-field-cooled (ZFC, blue) and field-cooled (FC, red) data are presented. The inverse susceptibility is plotted as a function of temperature for the ZFC data with a Curie-Weiss fit (solid green lines).

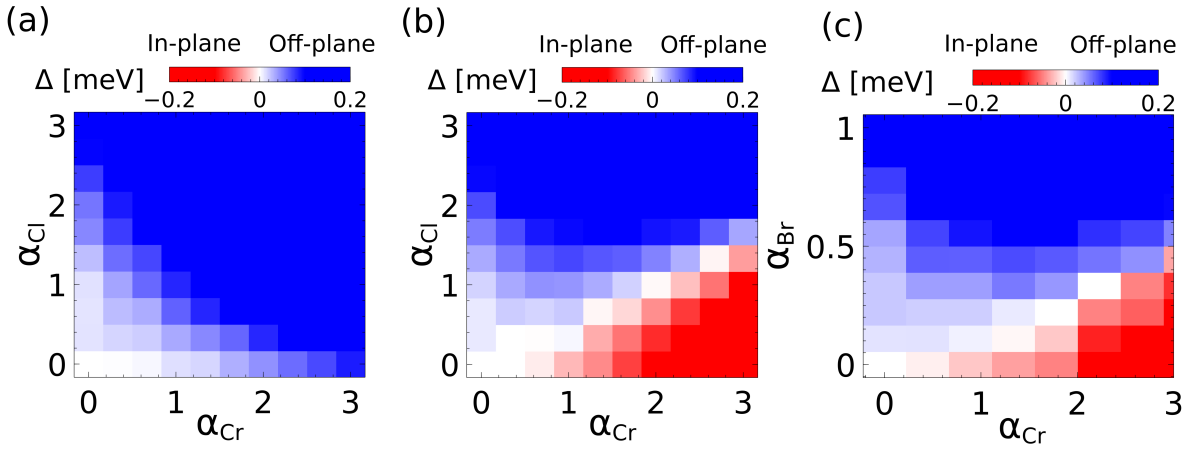

Figure S4: **Theoretical verification of the magnetic anisotropy.** Magnetic anisotropy energy as a function of the spin-orbit coupling (SOC) in Cr and Cl calculated for (a) the relaxed structure, and (b) 1% compressed structure of $CrCl_3$. Note that the relaxed structure shows only off-plane anisotropy which disagrees with the experimental findings, hence the need for lattice compression. (c) A similar calculation is performed for $CrBr_3$ where the off-plane anisotropy is much stronger due to the large SOC of Br.

structural relaxation within DFT to make our calculations self-consistent. Lattice relaxations were performed with Quantum Espresso (43), PBEsol functional, and PAW pseudopotentials. The DFT relaxed structure was consistent with the experimental lattice parameters; however, it was found to incorrectly predict an off-plane anisotropy in $CrCl_3$ (20), in stark contrast with the experimental findings (Fig. S4(a)). A wrong prediction of the magnetic anisotropy for $CrCl_3$ may result from the missing dipolar contribution to the anisotropy energy in DFT or from a limitation of conventional exchange correlation functionals (44). To circumvent these limitations, we applied a 2% compressive strain that yielded an in-plane anisotropy, in agreement with the experimental findings (see Fig. 5 in the main text).

Here, we present a similar calculation but with 1% lattice compression in Fig. S4(b). The result is improved compared to the bare DFT calculation in Fig. S4(a), but still not as good as the calculation with 2% compression in Fig. 5 of the main text. These calculations show the tendency toward off-plane anisotropy in $CrCl_3$ and the need to include a small compressive strain to obtain physical results. For completeness, we present a similar calculation (with 1% lattice compression) in $CrBr_3$, in Fig. S4(c), that reveals a much stronger off-plane anisotropy due to the large SOC of Br. Note that the y-scale in Fig. S4(c) is deliberately stopped at 1 to make sure the in-plane region (red) is visible.

Exfoliation

Here, we show that $CrCl_{3-x-y}Br_xI_y$ samples can be exofoliated just as well as their parent structures CrI_3, $CrBr_3$, and $CrCl_3$. Figure S5(a) shows an atomic force microscope (AFM) image of a thin flake after mechanical exfoliation. The box labeled (c) indicates the area for which height distribution is plotted in Fig. S5(c). The line labeled (d) indicates the path along which the profile in Fig. S5(d) is taken. The numbers (1) and (2) indicate the two flakes whose heights can be seen in Fig. S5(c). Figure S5(b) shows an optical image of the flake. The dotted box indicates the area of the AFM scan. Figure S5(c) shows the height distribution for the box

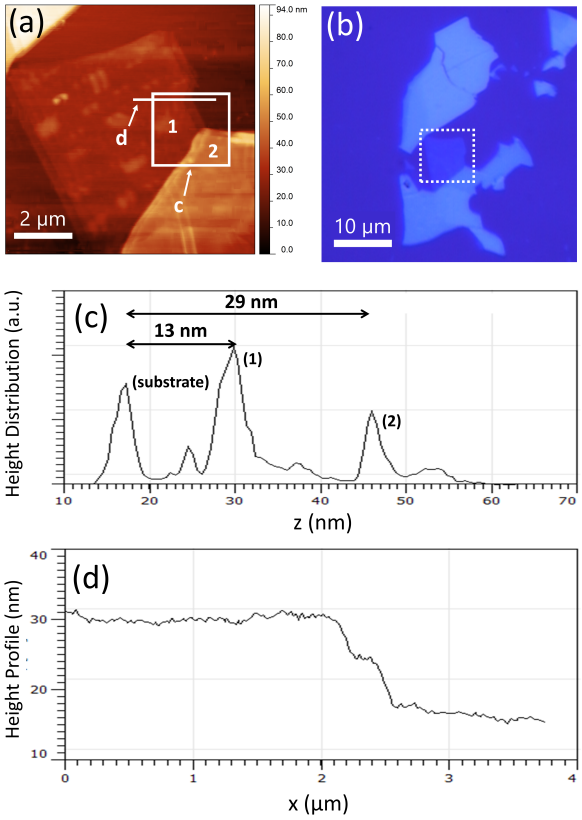

Figure S5: **Mechanical exfoliation of the VdW alloys.** (a) AFM image of an exfoliated sample with a thinner (1) and a thicker (2) flake. (b) Optical image of the exfoliated flakes on a Si/SiO_2 substrate. Panel (a) corresponds to the dotted square. (c) Height distribution of the flakes. (d) Height profile of the thinner flake in panel (a) along path d.

shown in Fig. S5(a). We can see three distinct peaks here – the first is the height of the substrate, the second is the height of region (1), the thinnest flake, and the third is the height of region (2), a thicker flake adjacent to the thin flake. Figure S5(d) shows the height profile for the line labeled (d) in Fig. S5(a). The drop-off in height corresponds to the edge of the thin flake and the flat tail beyond $x = 2.5$ μm corresponds to the substrate. The height of the flake appears to be approximately 13 nm.